Polskie Towarzystwo Materiałów Kompozytowych
Polish Society of Composite Materials

26: 1 (2026) 11–23

COMPOSITES THEORY AND PRACTICE

ISSN (online): 2299-128X

Priyadarshini Shivani Sahoo, Priyabrata Pattanaik, Satyanarayan Bhuyan, Jagadish Chandra Padhi

Faculty of Engineering and Technology, Siksha 'O' Anusandhan Deemed to be University, Bhubaneswar 751030, India
Correspondence: Priyadarshini Shivani Sahoo (priyadarshinisahoo@soa.ac.in)

Received (Otrzymano) 14.10.2025
Published on-line (Opublikowano) 31.03.2026

INVESTIGATION OF STRUCTURAL-MORPHOLOGICAL AND DIELECTRIC PROPERTIES OF $Bi_{1.7}La_{0.3}Ni_2Fe_2O_8$ MATERIAL FOR MULTIFUNCTIONAL DEVICE APPLICATIONS

https://doi.org/10.62753/ctp.2026.02.1.1

The innovative solid state step-sintering reaction technique was used to fabricate lanthanum doped bismuth-nickel ferrite perovskite oxide ($Bi_{1.7}La_{0.3}Ni_2Fe_2O_8$). The physical features, surface shape, grain dispersion topography, spatial frequency spectrum and temperature-frequency dependent dielectric properties were investigated. By means of X-ray diffraction, the W-H approach, SEM morphology, histograms and EDAX color mapping, the attributes of the produced material concerning crystallite size (47.5 nm), strain (0.00152), dislocation density(4.43×10^{14} m^{-2}), polycrystalline grain (0.01 µm-2µm) orientations, uniformly aligned grain texture, modest isotropy (50.45 %) and elemental compositions were evaluated. Impedance spectroscopy analysis of this material provides insight into the dielectric dispersion. The low dielectric loss in the high frequency regime signifies negligible dielectric energy dissipation. The findings support the idea that $Bi_{1.7}La_{0.3}Ni_2Fe_2O_8$ might be a promising mixed metal oxide-based ceramic component for potential multifunctional electronic device applications.

Keywords: $Bi_{1.7}La_{0.3}Ni_2Fe_2O_8$ material, electrical properties, dielectric spectrum

INTRODUCTION

The creation of sophisticated mixed metal oxide-based ceramic materials greatly influences the growth for digital appliances in the current technical breakthrough of ceramic manufacturing [1-2]. The exceptional electrical and magnetic properties of metal oxide-based complex perovskite ceramic materials, along with their physico-chemical stability and thermal-electrical-mechanical resistance, make them superior to other materials in industrial and research applications such as capacitors, data storage devices, dielectric substrates, energy harvesters, phase shifters, actuators, filters, transducers, sensors, photo-catalysis and spintronics [3-7]. Among other ceramics, mixed metal oxide-based bismuth ferrite $BiFeO_3$, has been considered as a potential entry into the electronics application segment because of its many striking and varied properties, including a resonance frequency that is thermally stable, a large phase dispersion, high voltage endurance, and low dielectric losses [8]. Despite its numerous benefits, the properties of mixed metal oxide-based bismuth ferrite $BiFeO_3$ when used to make an electronic device may be compromised due to its intrinsic issues, such as a high discharge current, a diminished magnetoelectric response, and structural distortion accompanied by tangent loss [9]. Thus, there has been an ongoing endeavor to achieve better electrical properties of $BiFeO_3$ by incorporating other atoms/additional elements on either the A or B sites,

which has been assumed to be another successful approach to change the properties. Prior research suggests that the emergence of secondary phases may be diminished by substituting isovalent elements or atoms at Bi-sites. The inherent ferroelectric properties, particularly their magnetic properties, have been impacted by the 6s2 lone pair discrepancy of bismuth [10–11]. On the other hand, isovalent substitution at the Fe-site modifies its magnetic properties without significantly changing its ferroelectric activity [12]. Conversely, the substitution of a different ionic charge than the atom it replaces at the Bi-site /or Fe-site creates oxygen vacancies, which ultimately improves the electrical properties [13]. Moreover, it has been reported that the partial substitution of ferromagnetic substances with nickel (Ni) in $BiFeO_3$ is very beneficial since it modifies the dielectric response, thereby establishing it as a promising material for advanced electronic device applications because Ni^{2+} has a similar ionic radius to Fe^{3+}. The incorporation of nickel at the Fe-site can lessen leakage by lowering oxygen vacancies, and enhances the piezoelectric, ferromagnetic and ferroelectric properties [14-17]. Despite the fact that research inquiries have been conducted on rare earth substituted bismuth ferrite based complex ceramics [18-19], there has not been any thorough study done on the use of rare earth lanthanum with the incorporation of equal proportions of nickel at the B-site (Fe-site) without altering the A-site (Bi-site). The equal proportions of Ni and Fe occupying the Fe-site allow the material to be regarded as a double perovskite-like derivative of $BiFeO_3$, which may alter the dielectric properties due to the following exchange: (Fe–O–Fe → Fe–O–Ni / Ni–O–Ni). The substitutions of La^{3+} at the Bi^{3+} site can suppress oxygen vacancies and enhance phase purity, while Ni^{2+} at the Fe^{3+} site can strengthen the magnetic exchange interactions. The combined effect can result in enhanced structural stability and dielectric properties. Thus, there is a great deal of interest in lanthanum doped bismuth-nickel ferrite perovskite oxide based lead-free dielectric components, which offer an environmentally friendly alternative for use in multifunctional electronic device applications.

In the present study, a lanthanum (La^{3+}) substituted bismuth based mixed metal oxide ceramic, $Bi_{2(1-x)}\ La_xNi_2Fe_2O_8$ with x = 0.3, was fabricated from Bi_2O_3, Fe_2O_3, La_2O_3 and NiO utilizing a new step-sintering procedure for the solid-state mixed oxides process for raw materials. Compared to alternative synthesis techniques, the described step-sintering synthesis method for mixed oxides in solid state at lower temperatures is simple to use, adaptable, and sustainable. Experimental research and thorough analysis were successfully conducted to reveal the structural features, morphology, surface topography and temperature dependent frequency dispersion spectra in order to validate the processed material as a suitable dielectric component for advanced electronic applications.

PREPARATION OF SAMPLES FOR CHARACTERIZATION

The lanthanum doped bismuth-nickel ferrite perovskite oxide ceramic sample ($Bi_{1.7}La_{0.3}Ni_2Fe_2O_8$) was produced by a traditional solid-state reaction process with bismuth(III) oxide (Bi_2O_3), lanthanum(III) oxide (La_2O_3), nickel(II) oxide (NiO), and ferric oxide (Fe_2O_3) powders as analytical grade raw materials (> 99.9 %) supplied by Pvt. Ltd. Loba Chemicals in India. It followed this basic chemical reaction

$$0.85Bi_2O_3+0.15La_2O_3+2NiO+Fe_2O_3 \longrightarrow Bi_{1.7}\,La_{0.3}Ni_2Fe_2O_8 \quad (1)$$

These raw oxides were combined together in the following molecular weight % ratios: 52.54:6.48:19.81:21.17. This resulted in a homogeneous mixture. After that, it was dry milled for around five hours. 75 ml of pure methanol (70 vol%) was added, and the mixture was ground wet until all the methanol evaporated. This produced a fine powder that was evenly mixed. It took about five hours for the whole evaporation process to finish. Following that, the material was put in an alumina crucible and heated to 800°C for 6 hours in a muffle furnace. The fabrication procedure is shown in Figure 1. After the calcination process was completed, the calcined material was ground up again to obtain a homogeneous ceramic mixture and subsequently subjected to X-ray diffraction (XRD) for structural characterization. The scanning rate was 2°/min, optical wavelength 1.5405 Å, and the Bragg angle range was $20° < 2\theta < 80°$.

After that, a binder, PVA (polyvinyl alcohol), was added to the calcined powder and combined extremely thoroughly to produce granules. The granulated powder was uniaxially pressed into round discs (10 mm × 2 mm) for 3 minutes at the pressure of 5 × 106 N/m² using a hydraulic press. The discs were then sintered on an alumina boat for four hours at 850°C. Subsequent to the sintering process, the surfaces of the discs were polished with 1000 grade emery paper. To perform various electrical tests, an analytical grade silver paste was utilized as electrodes on two sides. Afterwards, by utilizing a ZM-2376 LCR meter from the NF Corporation, the relative permittivity including the dielectric loss parameters was evaluated at different frequency and temperature ranges.

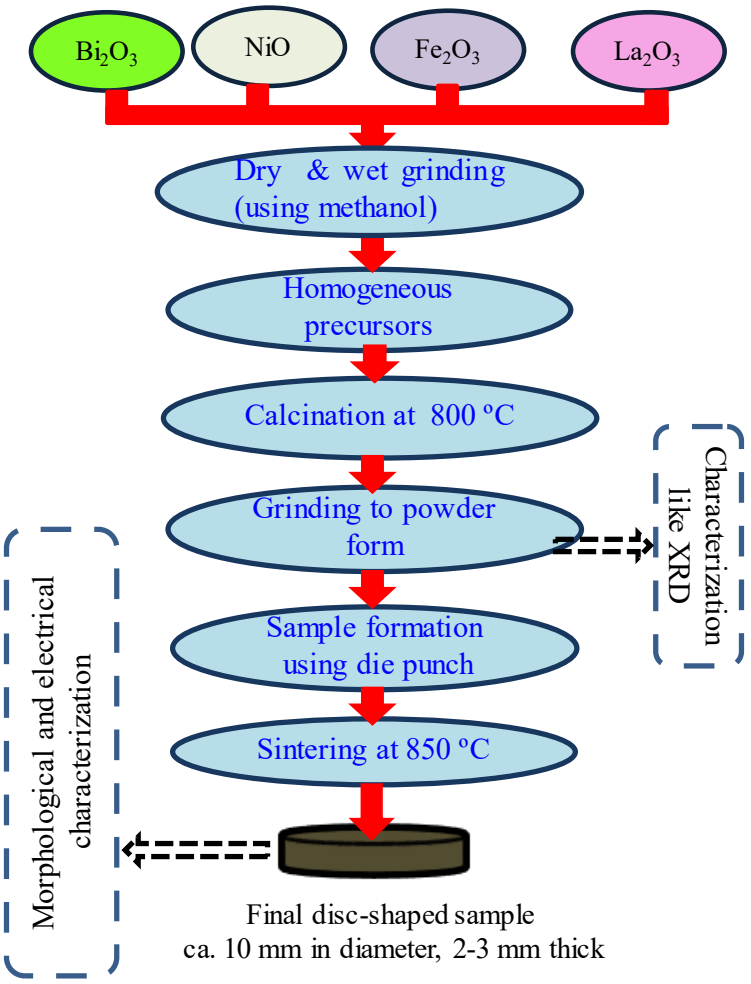

Fig. 1. Flowchart for fabrication of $Bi_{1.7}La_{0.3}Ni_2Fe_2O_8$ sample

IN-DEPTH EVALUATION AND INTERPRETATION OF RESULTS

Structural characterization using XRD

The structural features of the $Bi_{1.7}La_{0.3}Ni_2Fe_2O_8$ powder sample displayed in Figure 2 were obtained by XRD. The characteristics of the material can be observed with regard to the crystallite size, strain, and crystal structure. The polycrystalline nature was confirmed by applying the X'Pert High Score program to index the Miller indices of sharp peaks.. The XRD peaks were indexed according to cubic $Bi_{12.5}Fe_{0.5}O_{19.5}$ (JCPDS file #01-077-0865), cubic $FeLaO_3$ (JCPDS file #01-075-0541) and tetragonal $Fe_{1.966}O_{2.963}$(JCPDS file #01-089-5894) ceramics.

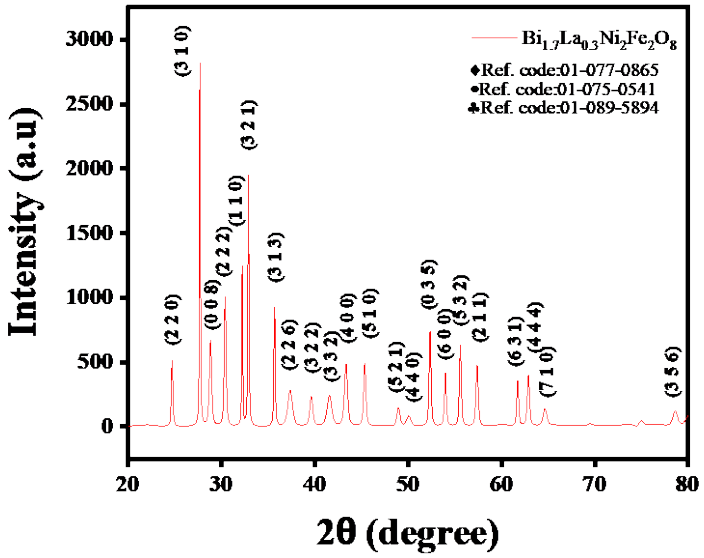

Fig. 2. XRD pattern of $Bi_{1.7}La_{0.3}Ni_2Fe_2O_8$

The following is a calculation of the crystallite size (T) applying the formula by Debye-Scherrer [20] and the subsequent formula for dislocation density (d):

$$T = \frac{P\lambda}{\beta \cos\theta} \quad \text{and} \quad d = \frac{1}{T^2} \tag{2}$$

where, P stands for the geometrical factor = 0.9, λ = 1.5405 Å the X-ray wavelength, θ the diffraction Bragg angle, and β full width at half maximum (in radians). The obtained values for dislocation density and crystallite size are 47.5 nm and 4.43×10^{14} m^{-2}, respectively.

Williamson-Hall approach

The W-H method examines the slope and intercept of the 4sinθ vs. βcosθ plot, as seen in Fig. 3, which effectively determines the material's microstrain and characteristic crystallite size.

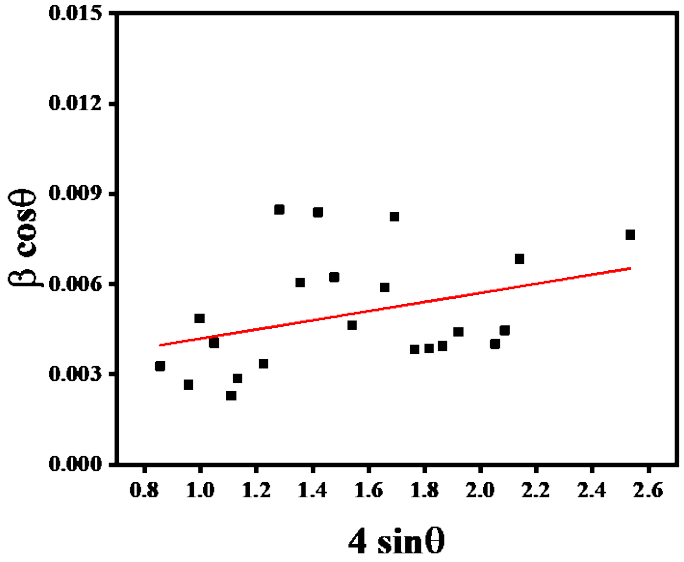

Fig. 3. W-H plot of $Bi_{1.7}La_{0.3}Ni_2Fe_2O_8$ ceramic

The graph in the figure shows the FWHM of the diffraction peaks plotted in comparison to the angle or scattering vector. By concurrently taking into account the impact of size and strain, the W-H approach determines the broadening of the diffraction peaks [20]. The effects of defects and dislocations on the strain inside the crystal lattice are considered. The combined effects of the crystallite size and strain determine the complete broadening, which is expressed as $\beta_T = \beta_D + \beta\epsilon s$, where β_T is the overall peak broadening as a consequence of microstrain indicated by θ, and the developed strain is represented by ε. β_D denotes the broadening related to the size effects of the crystallites ($\beta_D = P\lambda/TCos\theta$), and $\beta_{\epsilon s}$ is the strain-induced broadening ($\beta\epsilon s = 4\epsilon tan\theta$). Using the Williamson-Hall relation $\beta_T Cos\theta = (P\lambda/T) + 4\epsilon sin\theta$, and comparing with the unwavering line equation: y=0.00267+0.00152x (shown in Fig. 3), the sample's crystallite size was determined to be 51.9 nm, and the slope represents strain ε or 0.00152, with a y-intercept ($P\lambda/T$) = 0.00267.

SEM topography analysis and morphology with polar histogram

Fig. 4(a) shows the SEM micrographs of the $Bi_{1.7}La_{0.3}Ni_2Fe_2O_8$ ceramic material. The micrograph of the sample shows that the surface of the disc is consistent and covered in random tiny grains of different shapes, exhibiting minimal porosity and only a few isolated open voids in localized regions. The samples were completely sintered at 850°C more than the temperature of calcination in order to make a compact microstructure and avoid any possible porosity on the sample surface. Distinct grain boundaries are visible, which vary in size and are polycrystalline. There is a noticeable variation in particle size, as shown by the histogram that shows how the particle sizes are spread out, based on the SEM micrograph of the ceramic material in Fig. 4(b). The particles are between 0.01 μm and 2 μm in size, with an average diameter of 0.946 μm. The homogeneous sintering and microstructural stability are confirmed by the grain-distribution topography, which shows a uniformly distributed grain network with distinct boundaries and little agglomeration. As shown in Fig. 4(c), the SEM micrograph of the ceramic displays a three-dimensional surface topography with a height range from valley to peak of 11.187 μm. This variation in hue denotes a surface that is quite rough and has noticeable ridges, troughs, and grains. A spectrum of surface heights shows natural roughness and grain boundaries. It is possible to use the semi-circular rose plot to look at directional defects, crystallographic orientation, and angular distributions. Figure 4(d) presents blue lines that show the size or frequency of features that are lined up at angles between 0° and 180°. The isotropy value of 50.48% indicates that the pattern is not very anisotropic. The moderate isotropy value reveals that the surface stiffness and grain texture of the material are all oriented in the same way. The three main directions – 66.01°, 36.74°, and 90° – match up with the grain and structural alignments in the mixed ceramics. Figure 4(e) displays a polar histogram that illustrates the material's crystalline microstructure and grain orientation. The width of each bin shows how the data is oriented in proportion to the average direction of all the orientations. The structure has a moderate orientation dependence, with its structural elements centered between 56.47° and 70.39°. The spectrum shown in Fig. 4(f), reveals a circular mean of 13.94°; the results indicate that the typical orientation lies near the 0° axis. With a mean resultant length of only 0.04595, the dataset is almost isotropic and shows minimal directional bias at 0.4058°, a concentration of angular distribution. Fig. 4(g) reveals that the wavelength of about 27.97 μm corresponds to the dominating spatial frequency of 0.0357 μm^{-1}. It is the speed at which the texture or intensity (brightness) varies over a surface or image is represented by the spatial frequency spectrum. This indicates that elements of this size are the most prominent on the surface. This dominating feature strongly contributes to the entire spectrum as its comparable magnitude is 1.156 μm^3.

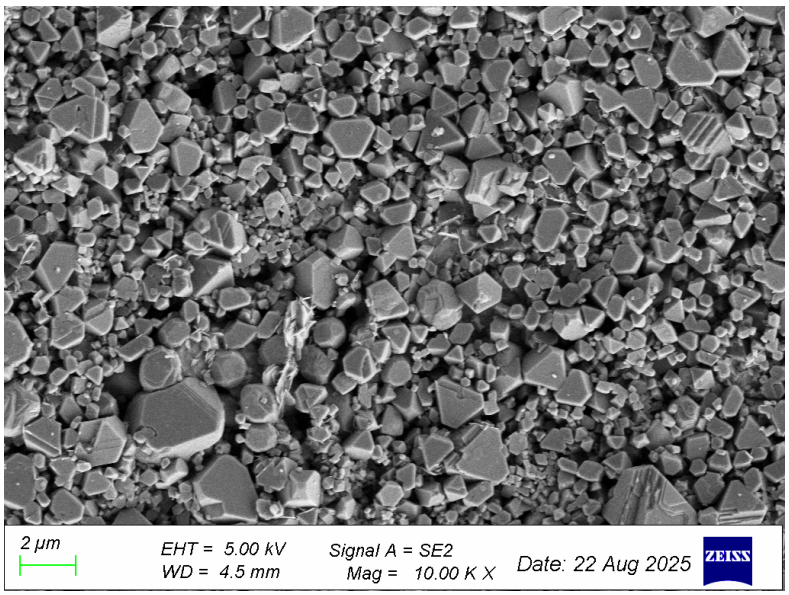

(a)

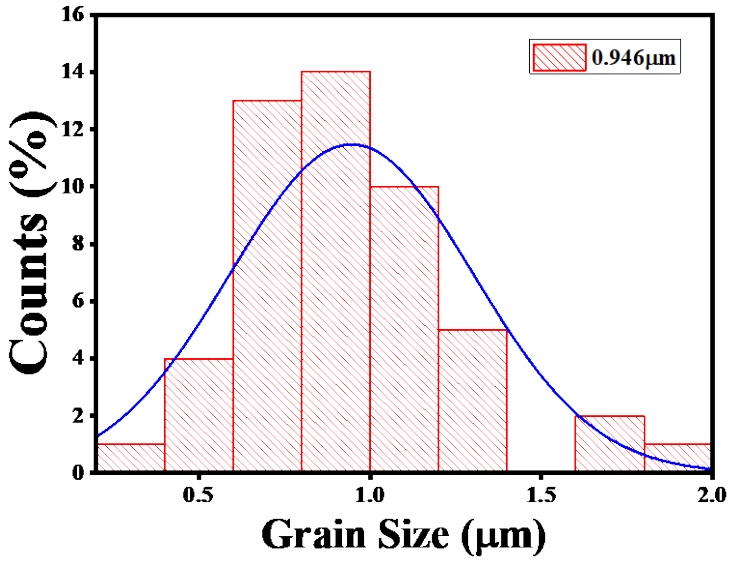

(b)

Fig. 4. (a) SEM micrograph, (b) histogram of particle sizes from SEM micrograph

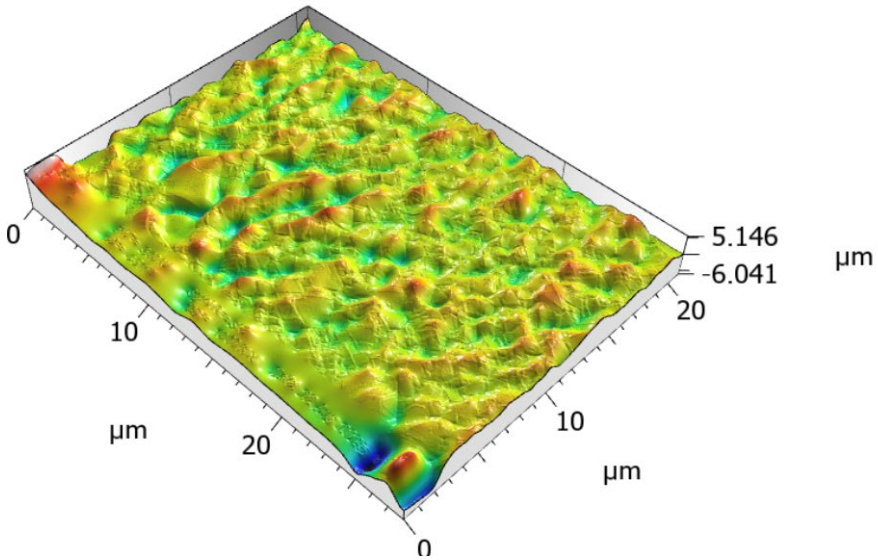

(c)

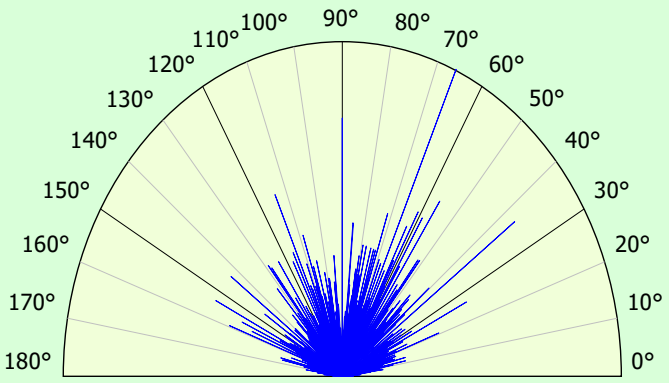

Parameters	Value	Unit	
Isotropy	50.45	%	
First direction	66.01	°	
Second direction	36.74	°	
Third direction	90.00	°	

(d)

Fig. 4. (c) micrograph surface, (d) texture-direction polar graph

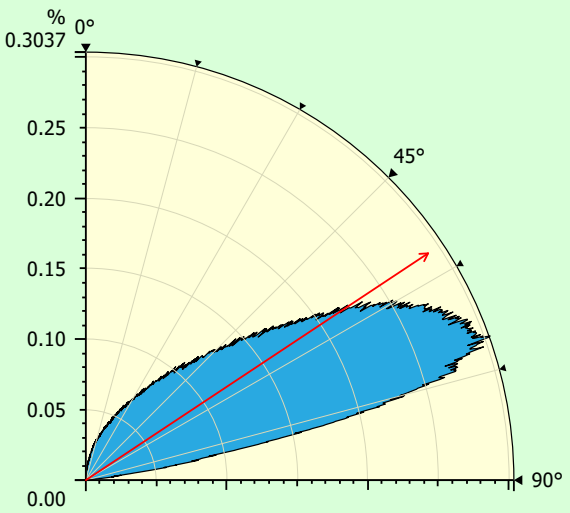

Information	
Angle	Polar angle (alpha)
Number of bins	887
Width of each bin	0.101466 °

Parameters	Value	Unit
Circular mean	56.47	°
Mean resultant length	0.9592	
Main	70.39	°

(e)

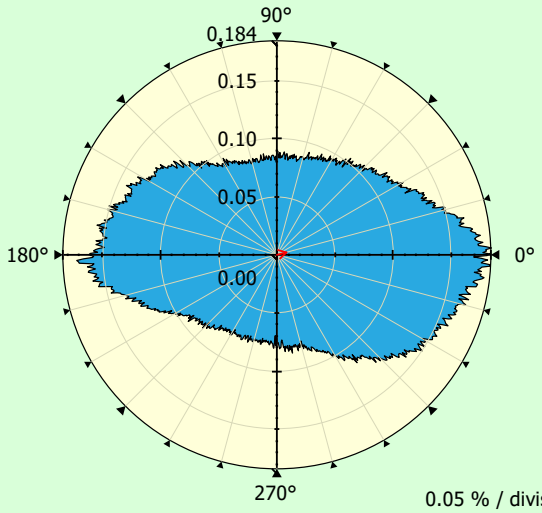

Information	
Angle	Azimuth angle (beta)
Number of bins	887
Width of each bin	0.405862 °

Parameters	Value	Unit
Circular mean	13.94	°
Mean resultant length	0.04595	
Main	1.524	°

(f)

Fig. 4. (e) SEM-generated polar histogram for grain orientation (f) azimuth angular distribution

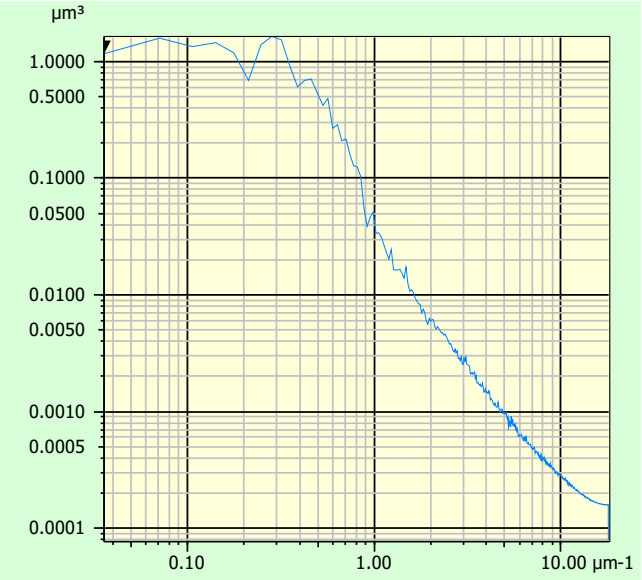

(g)

Fig. 4. (g) spatial frequency spectrum

EDAX spectrum with pie-chart for composition analysis

In order to determine the elemental composition of the $Bi_{1.7}La_{0.3}Ni_2Fe_2O_8$ material, an EDAX spectrum is used, as illustrated in Fig.5 (a). The x-axis indicates energy levels in keV, and the y-axis shows the X-ray intensity (counts), which is the number of photons recorded at each energy level. The color mapping in Fig. 5(b) shows that Bi, Ni, Fe, and O are oxides in the sample according to significant elemental spectrum peaks. The strong Fe K peak intensity indicates the dominance of iron in the sample. Oxides in the structure create the O K peak, confirming oxygen. The Bi M peak and Ni K peak represent bismuth and nickel in the sample. The spectrum also reveals no impurities in the ceramic. The elemental concentrations in $Bi_{1.7}La_{0.3}Ni_2Fe_2O_8$ (BLNFO) are shown in the pie chart in Fig. 5(c). The oxides are carefully selected for purity to manufacture polycrystalline BLNFO with Bi_2O_3, La_2O_3,Fe_2O_3 and NiO stoichiometrically: Bi (21.5 wt%, 4 at.%), La (7.4 wt%, 2.1 at.%), Ni (18.7 wt%, 12.5 at.%), Fe (27.1 wt% and 12.5 at.%), O (25.3 wt% and 62.3 at.%).

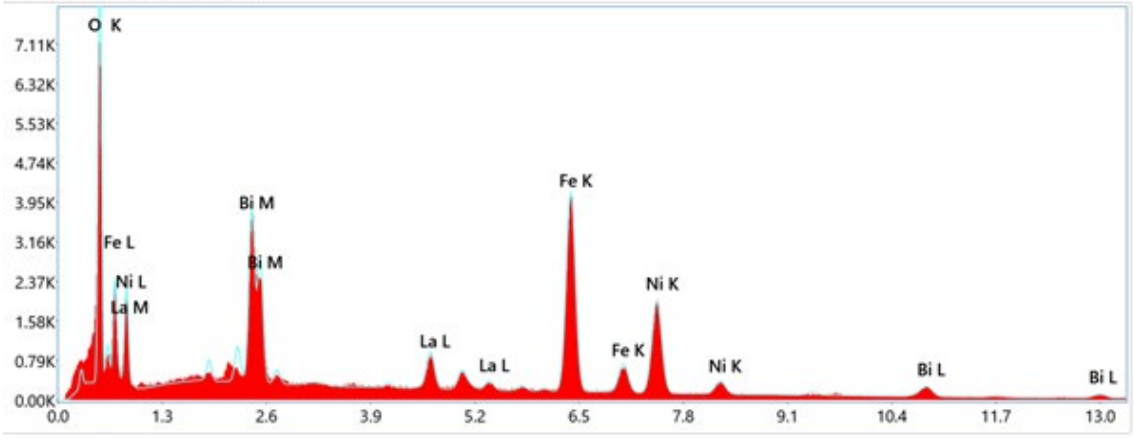

(a)

Fig. 5. (a) EDAX spectrum of $Bi_{1.7}La_{0.3}Ni_2Fe_2O_8$ ceramic

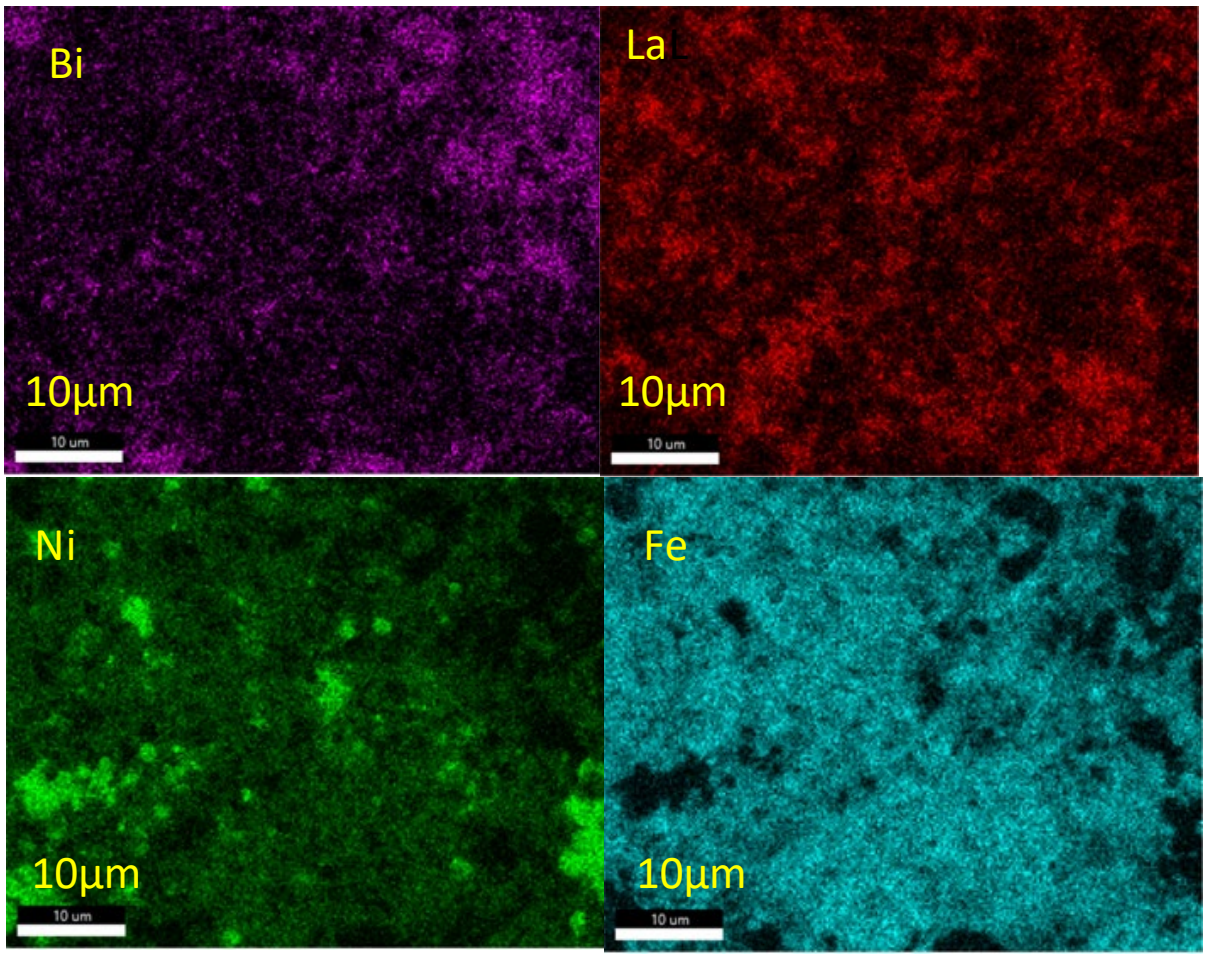

(b)

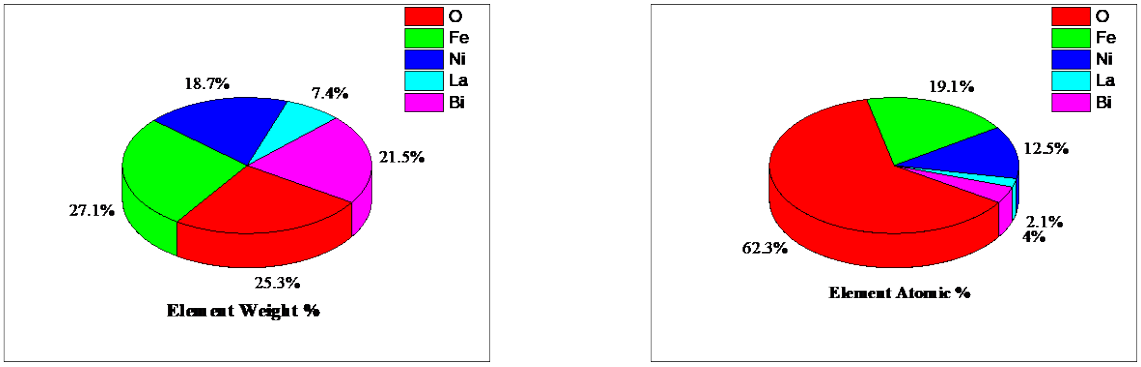

(c)

Fig. 5. (b) distribution of different elements, (c) concentration of individual elements of the ceramic in wt% and in at.%

Investigation of dielectric property with temperature-frequency dependency

The electrical activity of the sample was studied by means of impedance spectroscopy [21]. Using the LCR experimental setup, the dissipation factor and capacitance were determined. The findings of these measurements were then utilized to calculate the permittivity and loss tangent. Figure

6 illustrates how relative permittivity (ε_r) at particular frequencies changes with temperature, whereas Figure 7 shows the loss tangent (tanδ). Slowly growing with temperature, the ε_r curve becomes quite sharp at 410°C, which refers to the phase transition temperature owing to increased thermal agitation. The space charges collect at the grain boundary area when the temperature rises, creating oxygen vacancies and increasing the dielectric constant [22]. Oxygen vacancies facilitate increased polarization by raising defect-dipole production and local lattice deformation when exposed to an external electric field. The metal-oxygen-metal bonding network is weakened by the absent oxygen, which permits more off-center displacement of B-site cations. The overall polarization grows as a result of this increased ionic displacement.

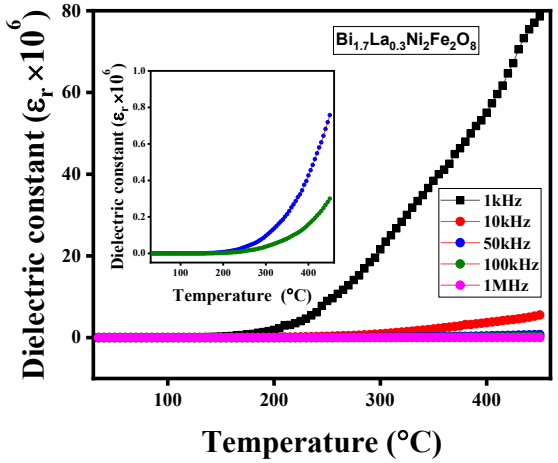

Fig. 6. Dielectric constant temperature dependency of $Bi_{1.7}La_{0.3}Ni_2Fe_2O_8$ at specific frequencies

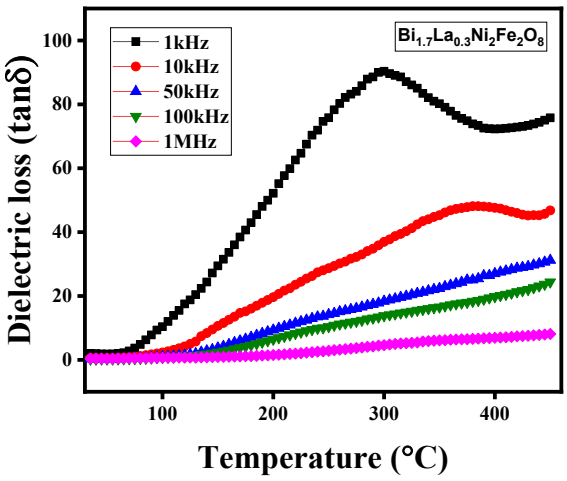

Fig. 7. Tangent loss temperature dependency of $Bi_{1.7}La_{0.3}Ni_2Fe_2O_8$ at specific frequencies

The temperature and frequency dependent variation of the dielectric constant (ε_r) was found to be comparable to the loss tangent (tanδ) features. The material's multiple polarizations cause the dielectric constant to grow during low frequency, which was initially demonstrated not to be affected by temperature (i.e. up to 220°C). Increasing the frequency causes this polarization effect to progressively diminish, which lowers the dielectric constant. With rising temperature, the value of εr climbs continuously up until it hits its peak, εmax, in the whole studied frequency range. The migration of space charges creates oxygen vacancies at high temperatures, which raises the relative dielectric constant [22]. At low temperatures, the rise of the loss tangent (tanδ) reduces because there are very few thermally generated charge carriers and no flaws or voids in the material, but it grows substantially in the high-temperature zone. Figures 8 and 9 show how εr as well as tanδ change for a given frequency in a dielectric sample across a temperature ranging from 35 to 400°C. Both properties drop with increasing frequency, which is a frequent feature of dielectric samples. The specimen's larger εr value in the low-frequency region might be due to electron build-up brought about by space charge polarization.

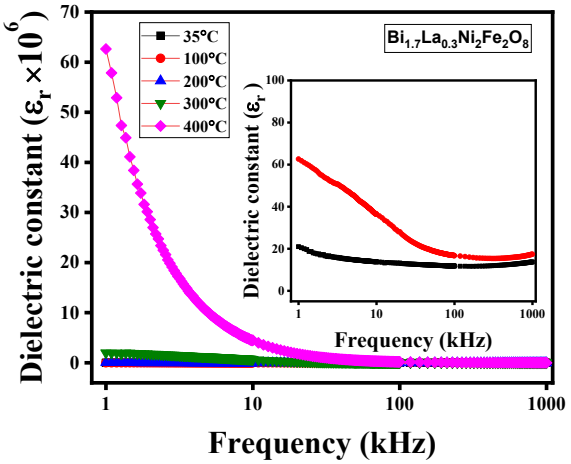

Fig. 8. Dielectric constant frequency dependency of $Bi_{1.7}La_{0.3}Ni_2Fe_2O_8$ at specific temperatures

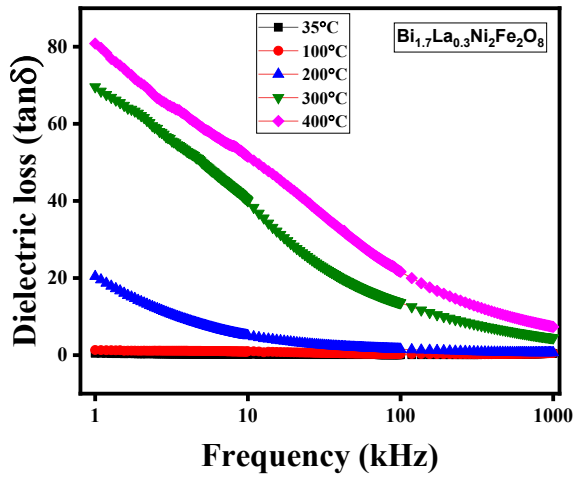

Fig. 9. Tangent loss frequency dependency of $Bi_{1.7}La_{0.3}Ni_2Fe_2O_8$ at specific temperatures

The frequency-tangent loss spectrum clearly illustrates that tanδ goes up quickly at low frequencies and down quickly at higher temperatures as the frequency rises. Koop's phenomenological theory and the Maxwell-Wagner phenomenon elucidate this specific dielectric behavior and may be applied to investigate the many polarization processes (atomic, ionic, dipolar, and interfacial) observed in this ceramic [23]. The accumulation of space charges, the movement of the electron cloud, the orientation of dipoles in the field direction, and the short-range separation of ions at low frequencies (100 Hz) all contribute to the high relative permittivity and dissipation factor. As the frequency falls, the whole polarization declines as well. At high frequencies, the minimum εr and tanδ are reached because only electrons can see the quick shift in frequency. At high frequencies, only electrons may perceive the sudden change in frequency. This makes the overall polarization dwindle as the frequency drops, which leads to the lowest values of εr and tanδ. Both the loss tangent and the dielectric constant show nearly frequency-independent responses in the high-frequency domain. This behavior results in practically constant εr and tan δ values because slower polarization mechanisms (space charge and dipolar contributions) can no longer follow the quickly oscillating field, leaving only the fast electronic/ionic polarization to contribute.

CONCLUSIONS

In the current study $Bi_{1.7}La_{0.3}Ni_2Fe_2O_8$ ceramic material was produced employing a mixed oxide low temperature cost effective solid-state reaction. The XRD analysis revealed the strain, crystallite size, and crystal structure. The W-H method accurately identified the material's typical crystallite size and micro-strain. SEM micrographs showed the polycrystalline microstructure composed of grains of variable sizes and well-defined grain boundaries. The element concentration was revealed by means of EDAX analysis and color mapping. Dielectric impedance spectroscopy was used to study how the produced sample behaves as a dielectric. This test method checks the material's permittivity and dissipation factor over a wide range of temperatures and frequencies. The experimental results validated the desired dielectric properties, indicating that the mixed metal oxide-based material $Bi_{1.7}La_{0.3}Ni_2Fe_2O_8$ may serve as a suitable ceramic substrate for the fabrication of capacitors, insulators, magnetic field sensors, and dielectric components for electronic circuit packaging.

REFERENCES

[1] K.S. Randhawa, Advanced ceramics in energy storage applications: Batteries to hydrogen energy, J. Energy Storage 98, 113122 (2024).

[2] M. Bhavisha, K. Anjali, S. Aswani, A. Sakthivel, Catalytic applications of perovskites, in Ceramic Catalysts, Elsevier, 19-55 (2023).

[3] P. V. C. K. Subhashini, K. V. D. Rajesh, Comparative performance assessment of nano-composite cathode of LMSO-BSCMF for low temperature solid oxide fuel cell applications, Composites Theory and Practice, 23: 4, 235-238, 2023.

[4] L. Sahoo, S. Bhuyan and S. N. Das, Tin oxide-titania based electronic system: synthesis, structural, microstructural and dielectric properties, Composites Theory and Practice 23: 4, 183-190, 2023.

[5] H. Esfanddarani, M. Panigrahi, Phytosynthesis of transition (Ni, Fe, Co, Cr, and Mn) metals and their oxide nanoparticles for biomedical applications: a review, J. Mater. Sci. 59(24), 10677-10723 (2024).

[6] S. Masih, N. Sharma, S. Kumar, A. Kaur, S. Middha, P.D. Babu, R. Ghosh, Flexible ceramic composites for magnetic field sensor applications, Ceram. Int. 51(5), 5790-5798 (2025).

[7] R. Muhamma, Y. Iqbal, and Ian M. Reaney, $BaTiO_3$–$Bi(Mg_{2/3}Nb_{1/3})O_3$ ceramics for high temperature capacitor applications, Journal of the American Ceramic Society, 99 (6), 2089-2095 (2016).

[8] G. Catalan, J. F. Scott, Physics and applications of Bismuth Ferrite. Adv Mater. 21:2463-85 (2009).

[9] Z. Sun, J. Wei, T. Yang, M. Xiahou, A. Cao, J. Zhang, Y. Yuanfeng, Y. He, Multifactorial coupling to greatly enhance photocurrent density of $BiFeO_3$-based ferroelectric photovoltaic architectures, J. Mater. Sci.: Mater. Electron. 35(31), 2035 (2024).

[10] S. K. Singh, K. Maruyama, H. Ishiwara, Reduced leakage current in La and Ni codoped $BiFeO_3$ thin films. Appl. Phys Lett. 91:112913-15 (2007).

[11] Dinesh Varshney, Ashwini Kumar, Kavita Verma, Effect of A site and B site doping on structural, thermal, and dielectric properties of $BiFeO_3$ ceramics, Journal of Alloys and Compounds, 509, 33, 8421-8426 (2011).

[12] J. Bielecki , P. Svedlindh, D. T. Tibebu, S. Cai, S. G. Eriksson, L. Borjesson, C. S. Knee Structural and magnetic properties of isovalently substituted multiferroic $BiFeO_3$: insights from Raman spectroscopy. Phys Rev B Condens Matter Phys. 86:184422 (2012).

[13] Jianguo Zhao, Xianghui Zhang, Shijiang Liu, Weiying Zhang, Zhaojun Liu, Effect of Ni substitution on the crystal structure and magnetic properties of $BiFeO_3$, Journal of Alloys and Compounds, 557, 120-123 (2013)

[14] Haiyang Dai, Fengjiao Ye, Zhenping Chen, Tao Li, Dewei Liu, The effect of ion doping at different sites on the structure, defects and multiferroic properties of $BiFeO_3$ ceramics, Journal of Alloys and Compounds, 734, 60-65 (2018)

[15] Tao li, Zhenping Chen, Investigations on the structure, defects, electrical and magnetic properties of Ni-substituted $BiFeO_3$ ceramics' Journal of Materials Science: Materials in Electronics, 27, 11, 11151-11157 (2016)

[16] C. Behera, R.N.P. Choudhary, P.R. Das, Structural and electrical properties of La-modified $BiFeO_3$–$BaTiO_3$ composites. J. Mater. Sci. Mater. Electron. 25, 2086-2095 (2014).

[17] A. Srivastava, A. K. Singh, O. N. Srivastava, H. S. Tewari, K. B. Masood, J. Singh, Magnetic and Dielectric Properties of La and Ni Co-substituted $BiFeO_3$ Nanoceramics, Frontiers in Physics, 8, (2020)

[18] Umer Waqas, Muhammad Umar Salman, Muhammad Ahmed Khan, Shahid M. Ramay, Farooq Ahmad, Saira Riaz, Shahid Atiq, Rapid switching capability and efficient magnetoelectric coupling mediated by effective interfacial interactions in $Bi0{\cdot}9La0{\cdot}1FeO_3/SrCoO_3$ bi-phase composites for ultra-sensitive pulsating devices, Journal of Materials Research and Technology, 29, 2971-2979 (2024).

[19] A. Srivastava, A. K. Singh, O. N. Srivastava, H. S. Tewari, B. Masood Khalid, J. Singh, Magnetic and Dielectric Properties of La and Ni Co-substituted $BiFeO_3$ Nanoceramics, 8, (2020).

[20] S. Kalingani, S.N. Das, S. Bhuyan, Structural, micro-structural, morphological, electrical spectroscopy and optical analysis of lithium–titanium oxide electronic material, Inorg. Chem. Commun. 159, 111731 (2024).

[21] K. Parida, S.K. Dehury, R.N.P. Choudhary, Structural, electrical and magneto-electric characteristics of $BiMgFeCeO_6$ ceramics, Phys. Lett. A 380, 4083-4091 (2016).

[22] P. Kumar, J.K. Juneja, C. Prakash, K.K. Raina, S. Singh, Effect of Sm on dielectric, ferroelectric and piezoelectric properties of BPTNZ system, Physica B 426, 112-117 (2013).

[23] S. Halder, S. Bhuyan, R.N.P. Choudhary, Structural, dielectric and electrical properties of bismuth magnesium tantalate electronic system, J. Magn. Alloys 7(4), 628-636 (2019).